AGU PUBLICATIONS

Geophysical Research Letters

RESEARCH LETTER
10.1002/2016GL069891

Key Points:
- The influence of complex 3-D wave propagation in the mantle on ScS_2/ScS amplitude ratios
- ScS_2-ScS difference times are delayed and ScS_2/ScS amplitude ratios are high on Samoa indicating low wave speeds but no attenuation
- Body wave amplitudes may be useful for evaluating the accuracy of tomographic models and as complementary data in tomographic inversions

Correspondence to:
C. Chaves,
calbertochaves@gmail.com

Citation:
Chaves, C. A. M., and J. Ritsema (2016), The influence of shear-velocity heterogeneity on ScS_2/ScS amplitude ratios and estimates of Q in the mantle, *Geophys. Res. Lett.*, *43*, 7997–8005, doi:10.1002/2016GL069891.

Received 3 JUN 2016
Accepted 23 JUL 2016
Accepted article online 27 JUL 2016
Published online 15 AUG 2016

The influence of shear-velocity heterogeneity on ScS_2/ScS amplitude ratios and estimates of Q in the mantle

Carlos A. M. Chaves[1,2] and Jeroen Ritsema[1]

[1]Department of Earth and Environmental Sciences, University of Michigan, Ann Arbor, Michigan, USA, [2]Departmento de Geofísica, Instituto de Atronomia and Geofísica e Ciências Atmoféricas, Universidade de São Paulo, São Paulo, Brasil

Abstract Regional waveforms of deep-focus Tonga-Fiji earthquakes indicate anomalous traveltime differences (ScS_2-ScS) and amplitude ratios (ScS_2/ScS) of the phases ScS and ScS_2. The correlation between the ScS_2-ScS delay time and the ScS_2/ScS amplitude ratio suggests that shear wave apparent Q in the mantle below the Tonga-Fiji region is highest when shear wave velocities are lowest. This observation is unexpected if temperature variations were responsible for the seismic anomalies. Using spectral element method waveform simulations for four tomographic models, we demonstrate that focusing and scattering of shear waves by long-wavelength 3-D heterogeneity in the mantle may overwhelm the signal from intrinsic attenuation in long-period ScS_2/ScS amplitude ratios. The tomographic models reproduce the trends in recorded ScS_2-ScS difference times and ScS_2/ScS amplitude ratios. Although they cannot be ruled out, variations in shear wave attenuation (i.e., the quality factor Q) are not necessary to explain the data.

1. Introduction

Wave attenuation measurements complement wave speed constraints on the thermal structure and the distribution of melts and fluids in the mantle [e.g., *Karato*, 1993; *Faul and Jackson*, 2005; *Karato and Jung*, 1998]. However, the modeling of seismic wave attenuation is difficult because wave scattering and defocusing (i.e., extrinsic attenuation) can have an equally large effect on waveforms [*Shearer*, 2015]. Strong horizontal contrasts near plate boundaries and continental margins may modify surface wave amplitudes [e.g., *Lay and Kanamori*, 1985; *Ji et al.*, 2005]. Corrections for multipathing are therefore essential in global surface wave attenuation tomography [e.g., *Dalton et al.*, 2008; *Ruan and Zhou*, 2012]. In this paper, we show that long-wavelength heterogeneity in the deep mantle can also affect long-period body wave amplitudes, with similar implications for studies of attenuation in the deep mantle.

We focus on the seismic phases ScS and ScS_2 (e.g., ScSScS), which have been widely used in studies of whole-mantle attenuation. ScS and ScS_2 are shear waves that reflect off Earth's surface and the outer core (Figure 1a). At epicentral distances shorter than 20°, ScS and ScS_2 are recorded with high amplitudes at relatively low frequencies (i.e., $f < 50$ mHz) and without interference with signals from other major phases (Figure 1b). They traverse the crust and mantle almost vertically. It has therefore been assumed that long-period ScS and ScS_2 waveforms are insusceptible to multipathing and amplification by layering and heterogeneity in the lithosphere and deep mantle.

Numerous researchers have modeled the traveltime difference and the amplitude or spectral ratio of ScS_2 and ScS to estimate the average shear wave velocity and attenuation in the mantle between source and receiver [e.g., *Kovach and Anderson*, 1964; *Jordan and Sipkin*, 1977; *Nakanishi*, 1979; *Lay and Wallace*, 1983; *Gomer and Okal*, 2003; *Sipkin and Revenaugh*, 1994; *Souriau et al.*, 2012]. Here we address an intriguing observation from the study by *Kanamori and Rivera* [2015], who measured ScS_2/ScS amplitude ratios and ScS_2-ScS difference traveltimes using waveform data from global seismic network stations. They determined the ScS_2/ScS ratio to be anomalously high and the ScS_2-ScS difference traveltime to be anomalously delayed at seismic station AFI (Afiamalu, Western Samoa). This suggests that shear wave propagation along paths to AFI is, on average, slow and that long-period shear waves are not strongly attenuated. Recordings at NOUC (Port Laguerres, New Caledonia), about 2500 km to the west-southwest of AFI, indicate a mantle structure with high apparent attenuation and a high average wave speed.

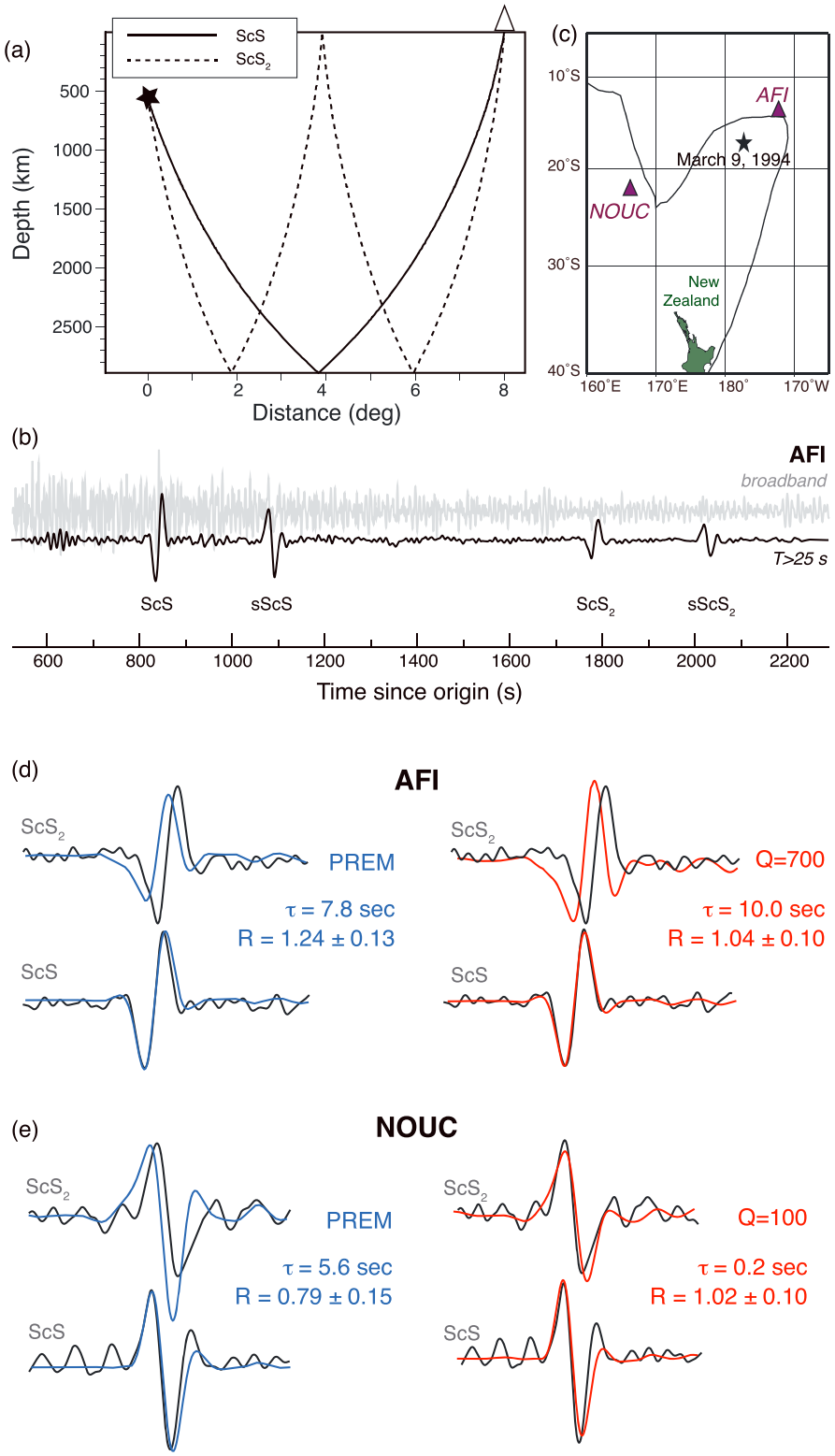

Figure 1. (a) Geometric ray paths of ScS (solid line) and ScS_2 (dashed line) for a distance of 8°. (b) Broadband (grey) and low-pass (T > 25 s)-filtered (black) radial component, ground-velocity recording of the 9 March 1994 earthquake (Event 1 in Table 1) at station AFI. (c) Location of stations AFI and NOUC (triangles) and Event 1 (star). (d and e) Estimates of the anomalies in the ScS_2-ScS difference time (i.e., τ) and ScS_2/ScS amplitude ratio (i.e., R) for stations AFI and NOUC. The waveforms in blue are for the Preliminary Reference Earth Model (PREM). The waveforms in red are for the best fitting Q models: $Q = 700$ for AFI and $Q = 100$ for NOUC.

Table 1. Global CMT Catalog Event Locations

Event	Date	Latitude (°S)	Longitude (°E)	H (km)	M_W
1	1994/03/09	17.7	−178.1	568	7.6
2	1998/03/29	17.6	−178.9	554	7.1
3	1998/05/16	22.3	−179.4	609	6.8
4	2004/07/15	17.7	−178.5	577	7.1
5	2006/01/02	19.8	−177.7	590	6.8
6	2009/11/09	17.1	178.5	604	7.3
7	2011/07/29	23.8	179.9	540	6.7
8	2011/09/15	21.6	−179.2	625	7.3
9	2013/05/23	23.2	−176.9	188	7.4
10	2014/07/21	19.7	−178.3	626	6.9
11	2006/01/02	19.8	−177.7	590	7.2

These observations are counterintuitive if temperature variations were responsible for the seismic anomalies. We address the apparent paradox by investigating whether 3-D shear-velocity structure imaged in four tomographic models can modify ScS and ScS_2 amplitudes using spectral element method simulations of waveforms.

2. ScS_2 and ScS Difference Times and Amplitude Ratios

2.1. Measurement

Following *Ritsema et al.* [2002], we estimate anomalies in the ScS_2-ScS traveltime difference and the ScS_2/ScS amplitude ratio by cross-correlating recorded (d) and synthetic (s) waveforms. The data are low-pass-filtered (T>25 s) horizontal-component recordings. The synthetics are computed using the AxiSEM method [*Nissen-Meyer et al.*, 2014], based on the PREM shear-velocity and Q structure [*Dziewonski and Anderson*, 1981]. We assume Global CMT source parameters [*Ekström et al.*, 2012] and convolve the synthetics with source time functions [*Vallée et al.*, 2011] to account for the effects of earthquake finiteness.

The delay time τ_{ScS} of ScS is determined from the maximum in the cross correlation between the recorded and computed ScS signals in a 80 s wide window W around the theoretical arrival time. M_1 and M_2 are estimates of the ratios of the recorded and computed ScS amplitudes. They are determined by ratios of cross-correlation and autocorrelation functions: $M_1 = d * s/s * s$ and $M_2 = d * d/d * s$. M_1 and M_2 minimize

$$\int_W \left[d(t) - M_1\, s(t-\tau)\right]^2 \, \mathrm{d}t \tag{1}$$

and

$$\int_W \left[M_2^{-1}\, d(t) - s(t-\tau)\right]^2 \, \mathrm{d}t. \tag{2}$$

$M_1 = M_2$ when the waveform d and s are identical. The difference between M_1 and M_2 is a measure of the least squares waveform misfit between d and s. Using windows around the ScS_2 signal, we estimate the delay time τ_{ScS_2} of ScS_2 and the ratios N_1 and N_2 between recorded and PREM-predicted ScS_2 amplitudes similarly.

The anomaly in the ScS_2-ScS difference traveltime is $\tau_{ScS2} - \tau_{ScS}$ and denoted as τ from here on. A value of $\tau = 0$ means that the assumed seismic model explains the recorded ScS_2-ScS traveltime difference perfectly. The anomaly in the ScS_2/ScS ratio with respect to the predicted ScS_2/ScS ratio is

$$R = \frac{1}{2}\left(\frac{\max(N_1, N_2)}{\min(M_1, M_2)} + \frac{\min(N_1, N_2)}{\max(M_1, M_2)}\right). \tag{3}$$

The uncertainty in R is

$$E = \frac{1}{2}\left(\frac{\max(N_1, N_2)}{\min(M_1, M_2)} - \frac{\min(N_1, N_2)}{\max(M_1, M_2)}\right). \tag{4}$$

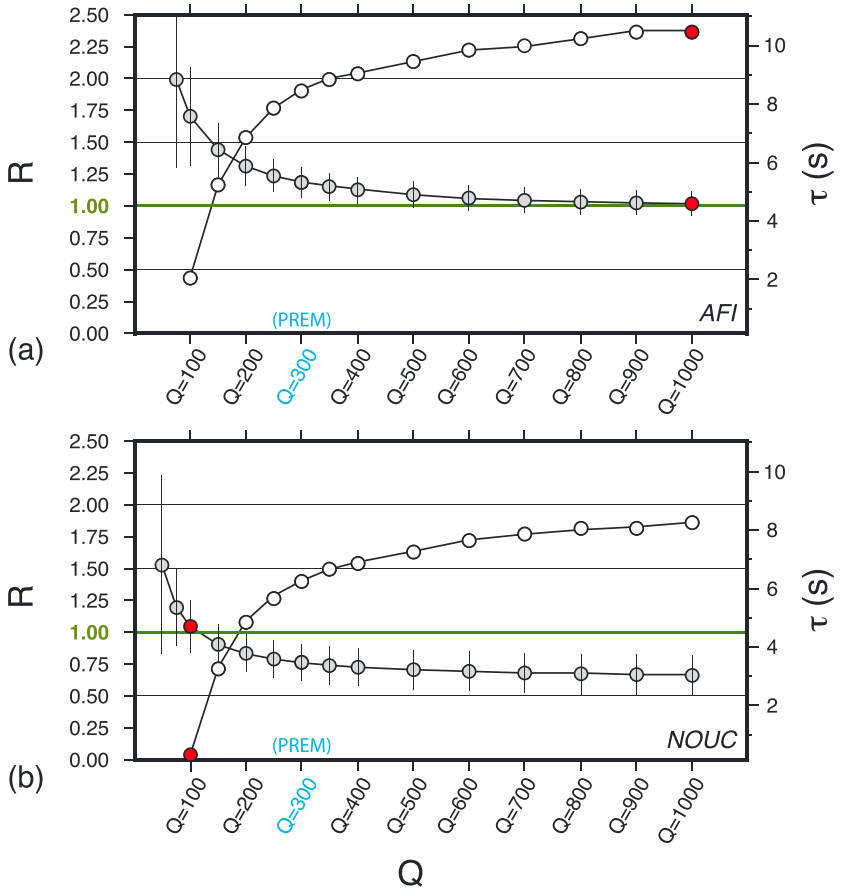

Figure 2. Measurements of R (grey circles) and τ (white circles) using radial-component waveforms at (a) AFI and (b) NOUC for the 9 March 2004 earthquake (Event 1 in Table 1). R and τ are estimated with respect to modified PREMs. In these models, Q in the mantle has been varied between $Q = 50$ and $Q = 1000$. The red circles indicate that the recorded ScS_2/ScS amplitude ratios is optimally matched when $Q = 1000$ for AFI and $Q = 100$ for NOUC.

τ and R are not affected by source mislocation and uncertainties in the seismic moment and the source mechanism. Amplitude decay due to geometric spreading is included in the synthetics.

2.2. The Quality Factor Q

The quality factor Q quantifies the loss of energy per wave cycle [e.g., *Stein and Wysession*, 2003]. The reduction of the ScS_2/ScS amplitude ratio is proportional to $\exp\left(-a\,Q^{-1}\right)$. The factor $a = \pi\ f\ \Delta t$, where f is signal frequency and Δt is the ScS_2-ScS traveltime difference of about 930 s. Since we analyze waveforms at a frequency of about $f = 1/30$ Hz, a has a value of about 100. Q in the PREM has an average value of about 300. As an anomaly with respect to PREM, R depends on the true average Q value for the mantle as $\log R = 0.33 - 100/Q$. R is about 1.26 when $Q = 1000$ and R is about 0.72 when $Q = 150$ in the mantle.

2.3. Examples From AFI and NOUC

We select waveform data from 11 deep earthquakes (Table 1). Deep earthquakes generate simple body wave signals that are not complicated by interference with the free surface reflections (sScS and $sScS_2$ in this case).

Figures 1d and 1e illustrate the measurements of R and E for the recordings of the 9 March 1994, M_W 7.6 Tonga earthquake (Event 1 in Table 1) at stations AFI and NOUC (Figure 1c). The phases ScS and ScS_2 (and the surface reflections sScS and $sScS_2$) emerge as high-amplitude signals after low-pass filtering the broadband recordings (T>25 s). For AFI, the anomaly τ in the ScS_2-ScS difference time is 7.8 s and the anomaly R in the ScS_2/ScS amplitude ratio is 1.24 ± 0.13 with respect to PREM. The ScS_2/ScS ratio is lower than the value predicted by PREM for station NOUC: $R = 0.79 \pm 0.15$.

The high ScS_2/ScS ratio at AFI alludes to low shear wave attenuation in the mantle between event 1 and AFI. Model Q700, which includes the PREM shear-velocity structure but assumes a constant quality factor

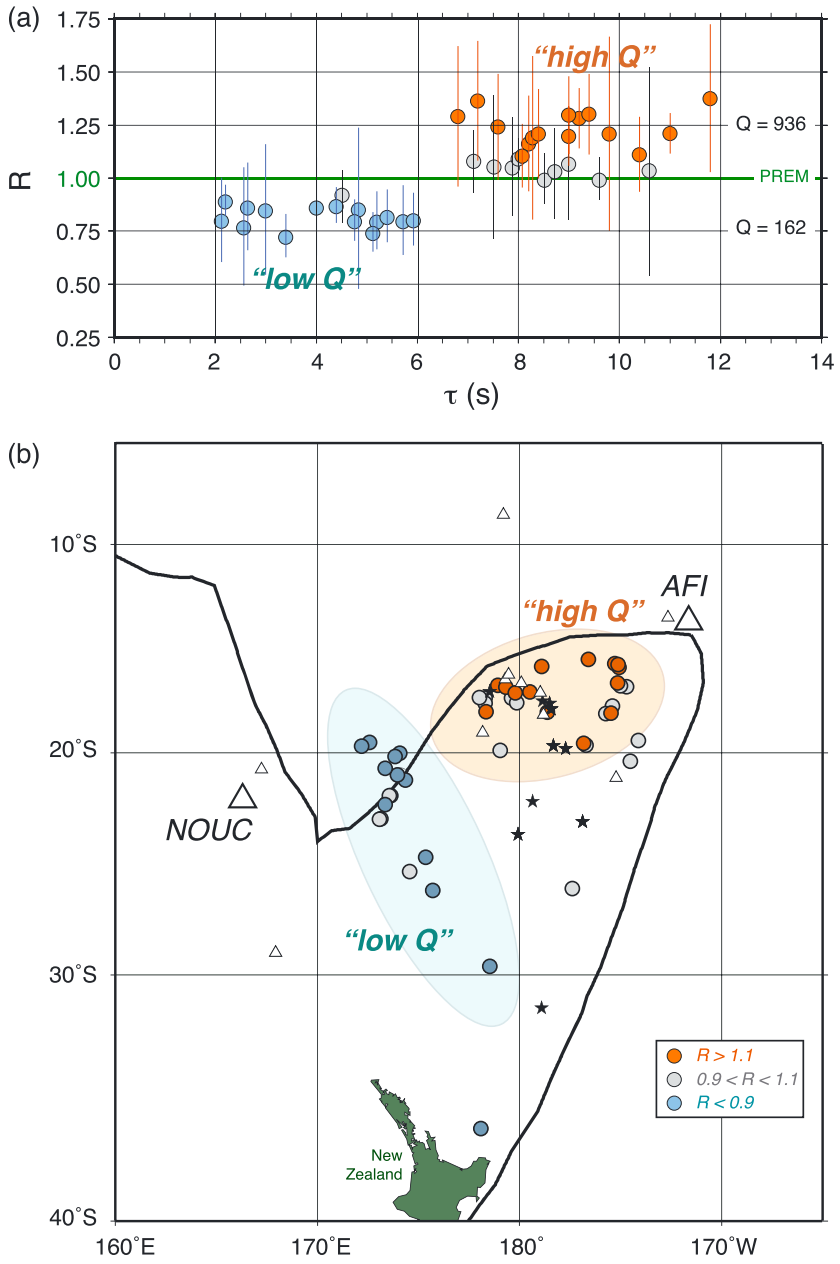

Figure 3. Measurements of R and τ with respect to PREM. Orange and blue circles indicate values $R > 1.1$ and $R < 0.9$, respectively. Grey circles indicates $0.9 < R < 1.1$. (a) R is plotted against τ. (b) R is plotted at the midpoints between events and stations. The data are based on recordings from events (stars) listed in Table 1 and broadband stations (triangles) in the region. The light blue and light brown ellipses encircle the low and high R ratios (i.e., the "low-Q" and "high-Q" regions), respectively.

$Q = 700$ throughout the mantle, explains the recorded ScS_2/ScS amplitude ratio within uncertainty (i.e., $R = 1.04 \pm 0.10$). The relatively low uncertainty E of 0.10, compared to 0.13 for PREM, indicates that the waveform fits of ScS_2 and ScS also improved when Q is assumed to be higher than in PREM. The ScS_2-ScS difference time anomaly of $\tau = 10.4$ s is slightly higher for Q700 than PREM ($\tau = 7.8$ s) since physical dispersion is smaller when Q is higher. For station NOUC, the ScS_2/ScS ratio is lower than the value predicted by PREM: $R = 0.79 \pm 0.15$. This low value of R suggests a lower apparent Q, and we find that values of about 100 fit the data well.

Figure 2 shows estimates of τ and R for recordings of event 1 at NOUC and AFI for models Q50 through Q1000 with the PREM shear-velocity structure and constant Q values in the mantle that vary between 50 and 1000. The recorded ScS_2/ScS amplitude at AFI is 25% higher than predicted by PREM. Despite the uncertainty in R, a

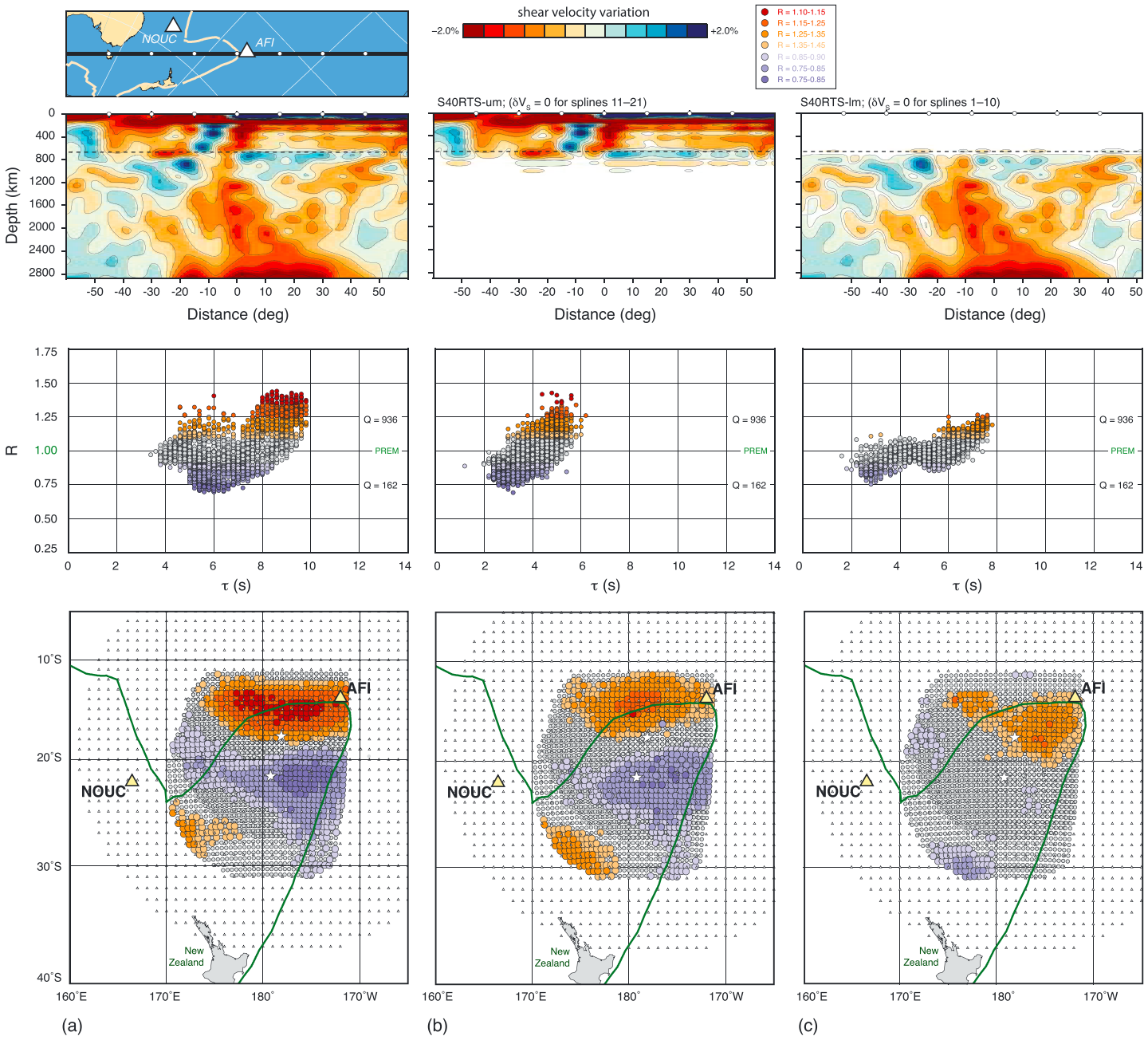

Figure 4. Measurements of R and τ using computed waveforms for three 3-D models: (a) S40RTS, (b) S40RTS but the PREM structure in the lower mantle, and (c) S40RTS but the PREM structure in the upper mantle. The top panels show the 3-D models in a cross section through event 1 and station AFI (see Figure 1). The middle panels show R versus τ. The bottom panels show R plotted at the midpoints between events and stations as in Figure 3. The waveforms are computed for events 1 and 8 from Table 1 at a grid of stations with a 1° × 1° spacing and within a distance of 20° from Events 1 and 8. The measurements are color coded according to the values of R, as indicated by the legend.

significantly better fit to the recorded ScS_2/ScS amplitude ratio at AFI is obtained when the average value of Q in the mantle is higher than 500. The ScS_2/ScS ratio at station NOUC is matched optimally (i.e., $R = 1$) when Q ranges from 75 to 150. This indicates that average shear wave attenuation is stronger toward the southwest. As physical dispersion in a model with $Q = 150$ is stronger than in PREM with $Q = 300$, the estimated ScS_2-ScS difference time anomaly τ is 2 s lower than for the PREM.

2.4. Multiple Event Observations

Figure 3 shows the measurements of τ and R (with respect to PREM) for all events from Table 1. The high values of R of about 1.25 are associated with values of τ larger than 7 s (Figure 3a). When interpreted as anomalies

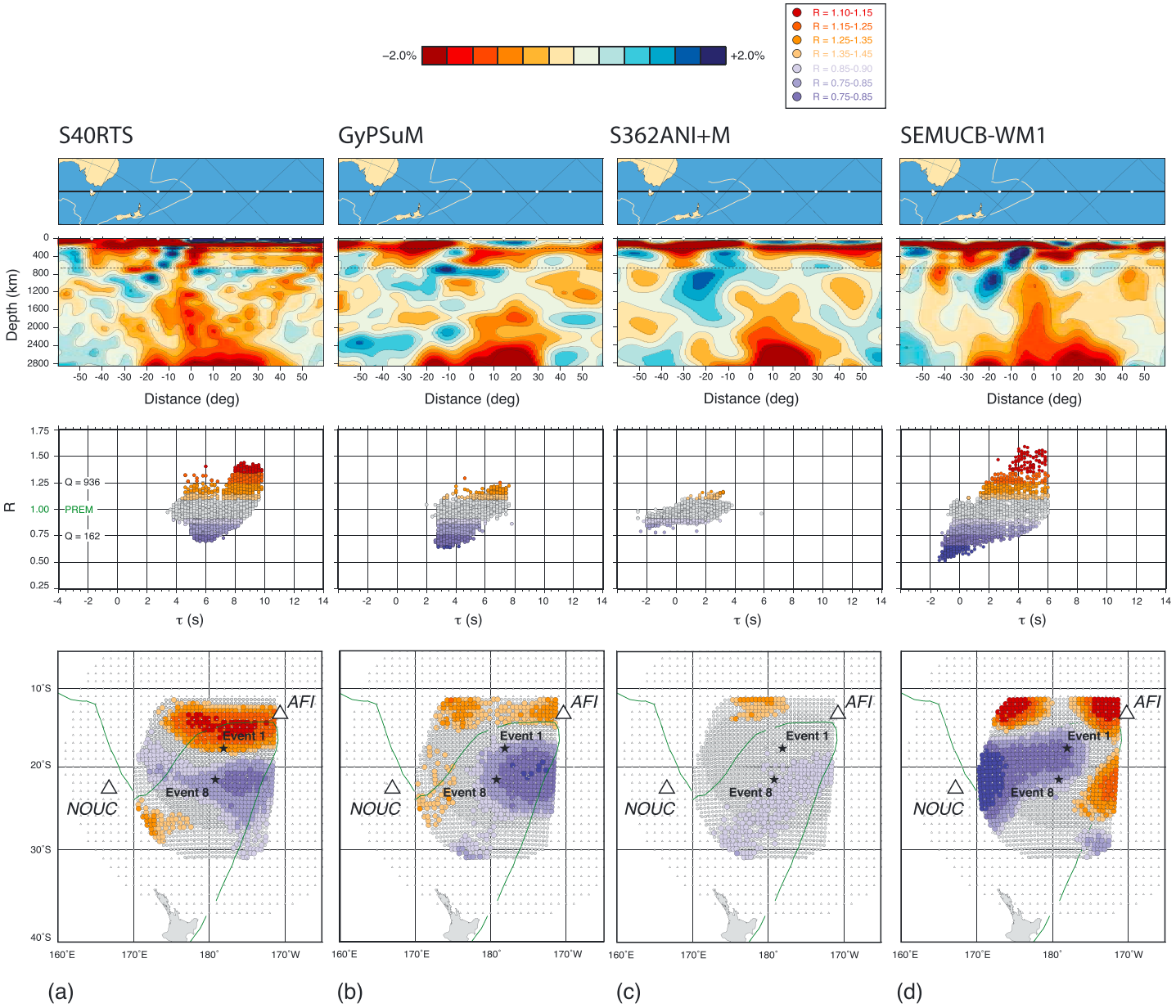

Figure 5. Measurements of R and τ using computed waveforms for four global tomographic models: (a) S40RTS [*Ritsema et al.*, 2011], (b) GyPSuM [*Simmons et al.*, 2010] (c) S362ANI+M [*Moulik and Ekström*, 2014], and (d) SEMUCB-WM1 [*French and Romanowicz*, 2014]. See the caption of Figure 4 for detail. Note that the τ axis in the middle panel is different than in Figure 4.

in shear velocity and shear attenuation, the correlation between R and τ means that shear wave attenuation is lowest, or Q is highest, in the mantle where shear-velocity reductions are strongest. The values of R plotted at the ScS core-mantle-boundary reflection points (Figure 3b) are separated in two regions as indicated by sketched ellipses. The highest values of R are obtained in the northernmost part of the sampling region. The lowest values of R are obtained to the southeast.

3. Modeling With 3-D Shear-Velocity Models

Figure 4 shows the simulated values for τ and R for model S40RTS [*Ritsema et al.*, 2011] and two modifications of S40RTS. S40RTS-um and S40RTS-lm are identical to S40RTS, but velocity perturbation are removed in the lower mantle (in Figure 4b) or in the upper mantle (in Figure 4c). We estimate τ and R by applying the procedures from section 2 to synthetic waveforms computed with the spectral element method of *Komatitsch*

Table 2. Measured and Predicted Values for τ and R

	EVENT 1				EVENT 8			
	AFI		NOUC		AFI		NOUC	
	τ	R	τ	R	τ	R	τ	R
Data	7.8 s	1.24 ± 0.13	5.6 s	0.79 ± 0.15	8.6 s	0.99 ± 0.12	4.4 s	0.98 ± 0.09
S40RTS	9.6 s	1.32 ± 0.11	7.2 s	0.92 ± 0.06	9.0 s	1.12 ± 0.11	6.8 s	0.97 ± 0.06
GypSum	5.8 s	0.94 ± 0.06	6.4 s	1.13 ± 0.08	4.8 s	0.82 ± 0.04	6.2 s	1.13 ± 0.09
S362ANI-M	2.2 s	0.98 ± 0.01	0.8 s	0.98 ± 0.01	1.2 s	0.92 ± 0.01	0.0 s	0.96 ± 0.01
SEMUCB-WM1	6.0 s	1.03 ± 0.02	0.8 s	0.77 ± 0.04	4.8 s	0.87 ± 0.05	0.1 s	0.70 ± 0.02

and Tromp [2002]. In these simulations, the Q structure is the same as in PREM. We simulate waveforms only for Events 1 and 8 from Table 1 for which we have the most observations. These two simulations are sufficient since the geographic patterns of R and correlation of τ and R are similar for events 1 and 8. To maximize geographic coverage, we determine τ and R using waveforms computed for a dense grid of stations.

For event 1, S40RTS predicts that $R = 1.32 \pm 0.11$ at AFI and $R = 0.92 \pm 0.06$ at NOUC. These values are consistent with the measurements in Figure 2. S40RTS (Figure 4a) underestimates the range in the recorded anomalies τ (4–10 s in S40RTS and 2–12 s in the data), but it reproduces the positive correlation between τ and R and the geographic variation of R shown in Figure 3.

Figures 4b and 4c demonstrate that S40RTS's heterogeneity in the upper and lower mantle contributes equally to τ and R. The broad shear-velocity anomaly in the lower mantle is responsible for the largest delays in the ScS_2-ScS difference time. The minimum in R originates from structure in the upper mantle. The maximum in R is due to structure in both the upper and lower mantle.

The data are too sparse to make a detailed comparison between the recorded and the computed values of τ and R. Nevertheless, the simulations indicate that the variations in τ and R can be explained by S40RTS without invoking variations of Q in the mantle.

Tomographic models GyPSuM [*Simmons et al.*, 2010], S362ANI+M [*Moulik and Ekström*, 2014] and SEMUCB-WM1 [*French and Romanowicz*, 2014] also predict variations in τ and R (Figure 5) due to shear-velocity heterogeneity but differ on the range of τ and R and the spatial variation of R. Table 2 compares the predicted values for τ and R and the estimated values from the recorded waveforms for Events 1 and 8 at stations AFI and NOUC. The differences underscore that the tomographic models do not agree in detail on the contribution from shear-velocity heterogeneity to τ and R.

4. Discussion and Conclusions

It is well understood that long-wavelength seismic velocity heterogeneity causes focusing and defocusing of seismic waves. Within the Tonga-Fiji region, anomalies in the ratio R of the ScS and ScS_2 amplitudes vary by up to a factor of 1.3. At periods longer than 25 s, the range of values for R are equivalent to Q variations between 100 and 700 as noted by *Kanamori and Rivera* [2015]. Tomography models of 3-D shear-velocity variations predict a similar variation albeit that the models differ in the magnitude and geographic variation of R. We cannot rule out that there are no variations of Q in the mantle. However, long-wavelength wave speed heterogeneity not only contributes significantly to anomalies in ScS_2/ScS; it may overwhelm the signal from attenuation. It is extremely difficult to quantify the effects of focusing and defocusing as demonstrated by the waveform simulations from Figure 5. The strength of resolved anomalies and velocity gradients in tomographic models remains too uncertain to make accurate corrections for the effects of shear-velocity on variations in wave amplitudes.

While the results in the paper underscore the difficulties of constraining shear wave attenuation from long-period waveforms such as ScS and ScS_2, body wave amplitudes may prove to be useful observables for evaluating the accuracy of tomographic models and as complementary data in tomographic inversions.

Finally, the measurements of wave delay times depend on the chosen Q structure in the background model (see Figure 2), as was previously pointed out by *Zhou* [2009], *Savage et al.* [2010], and *Ruan and Zhou* [2010]. Measurements of the traveltime delay of shear waves that propagate through the deep mantle, such as ScS

and ScS_2, can vary by as much as 2 s depending on the chosen Q structure. This is a significant fraction of recorded traveltime anomalies of up to 10–15 s. Unmodeled Q structure can bias tomographic inversions for shear-velocity heterogeneity.

Acknowledgments
Data have been provided by GEOSCOPE and IRIS. All figures were produced using the GMT software [*Wessel and Smith*, 1995]. This research has been supported by NSF grant EAR–1416695 and FAPESP grant 2014/17779–3. We thank Nathan Simmons and an anonymous reviewer for helpful comments. The authors acknowledge computing time provided on the Blue Gene/Q supercomputer supported by the CRC (Rice University) and LCCA (University of São Paulo) agreement. All data used in this study are available by contacting the corresponding author at calbertochaves@gmail.com.

References

Dalton, C. A., G. Ekström, and A. M. Dziewonski (2008), The global attenuation structure of the upper mantle, *J. Geophys. Res.*, *113*, B09303, doi:10.1029/2007JB005429.
Dziewonski, A. M., and D. L. Anderson (1981), Preliminary reference Earth model, *Phys. Earth Planet. Inter.*, *25*, 297–356.
Ekström, G., M. Nettles, and A. M. Dziewonski (2012), The global CMT project 2004–2010: Centroid-moment tensors for 13,017 earthquakes, *Phys. Earth Planet. Inter.*, *200–201*, 1–9, doi:10.1016/j.pepi.2012.04.002.
Faul, U. H., and I. Jackson (2005), The seismological signature of temperature and grain size variations in the upper mantle, *Earth Planet. Sci. Lett.*, *234*, 119–134.
French, S. W., and B. A. Romanowicz (2014), Whole mantle radially anisotropic shear-velocity structure from spectral-element waveform tomography, *Geophys. J. Int.*, *199*, 1303–1327, doi:10.1093/gji/ggu334.
Gomer, B. M., and E. A. Okal (2003), Multiple-ScS probing of the Ontong-Java plateau, *Phys. Earth Planet. Inter.*, *138*, 317–331.
Ji, C., S. Tsuboi, D. Komatitsch, and J. Tromp (2005), Rayleigh-wave multipathing along the West Coast of North America, *Bull. Seismol. Soc. Am.*, *95*, 2115–2124.
Jordan, T. H., and S. A. Sipkin (1977), Estimation of the attenuation operator for multiple ScS waves, *Geophys. Res. Lett.*, *4*, 167–170.
Kanamori, H., and L. Rivera (2015), Near-vertical multiple ScS phases and vertically averaged mantle properties, *Geol. Soc. Am. Spec. Pap.*, *514*, 9–31, doi:10.1130/2015.2514(02).
Karato, S. (1993), Importance of anelasticity in the interpretation of seismic tomography, *Geophys. Res. Lett.*, *20*, 1623–1626.
Karato, S., and H. Jung (1998), Water, partial melting and the origin of the seismic low velocity and high attenuation zone in the upper mantle, *Earth Planet. Sci. Lett.*, *157*, 193–207.
Komatitsch, D., and J. Tromp (2002), Spectral-element simulations of global seismic wave propagation—I. Validation, *149*, 390–412
Kovach, R. L., and D. L. Anderson (1964), Attenuation of shear waves in the upper and lower mantle, *Bull. Seismol. Soc. Am.*, *54*, 1855–1864.
Lay, T., and H. Kanamori (1985), Geometric effects of global lateral heterogeneity on long-period surface-wave propagation, *J. Geophys. Res.*, *90*, 605–621.
Lay, T., and T. C. Wallace (1983), Multiple ScS travel-times and attenuation beneath Mexico and Central-America, *Geophys. Res. Lett.*, *10*, 301–304.
Moulik, P., and G. Ekström (2014), An anisotropic shear velocity model of the Earth's mantle using normal modes, body waves, surface waves and long-period waveforms, *Geophys. J. Int.*, *199*, 1713–1738, doi:10.1093/gji/ggu356.
Nakanishi, I. (1979), Attenuation of multiple ScS waves beneath the Japanese Arc, *Phys. Earth Planet. Inter.*, *19*, 337–347.
Nissen-Meyer, T., M. van Driel, S. C. Stähler, K. Hosseini, S. Hempel, L. Auer, A. Colombi, and A. Fournier (2014), AxiSEM: Broadband 3-D seismic wavefields in axisymmetric media, *Solid Earth*, *5*, 425–445, doi:10.5194/se-5-425-2014.
Ritsema, J., L. A. Rivera, D. Komatitsch, J. Tromp, and H. J. van Heijst (2002), Effects of crust and mantle heterogeneity on PP/P and SS/S amplitude ratios, *Geophys. Res. Lett.*, *29*, 1430, doi:10.1029/2001GL013831.
Ritsema, J., H. J. van Heijst, A. Deuss, and J. H. Woodhouse (2011), S40RTS: A degree-40 shear velocity model for the mantle from new Rayleigh wave dispersion, teleseismic traveltime, and normal-mode splitting function measurements, *Geophys. J. Int.*, *184*, 1223–1236.
Ruan, Y., and Y. Zhou (2010), The effects of 3-D anelasticity (Q) structure on surface wave phase delays, *Geophys. J. Int.*, *181*, 479–492, doi:10.1111/j.1365-246X.2010.04514.x.
Ruan, Y., and Y. Zhou (2012), The effects of 3-D anelasticity (Q) structure on surface wave amplitudes, *Geophys. J. Int.*, *189*, 967–983, doi:10.1111/j.1365-246X.2011.05356.x.
Savage, B., D. Komatitsch, and J. Tromp (2010), Effects of 3D attenuation on seismic wave amplitude and phase measurements, *Bull. Seismol. Soc. Am.*, *100*(3), 1241–1251, doi:10.1785/0120090263.
Shearer, P. M. (2015), 1.24 Deep Earth structure: Seismic scattering in the deep Earth, in *Treatise on Geophysics, 2nd ed.*, edited by G. Schubert, pp. 759–781, PM Shearer Univ. of California, San Diego, La Jolla, doi:10.1016/B978-0-444-53802-4.00045-2.
Simmons, N. A., A. M. Forte, L. Boschi, and S. P. Grand (2010), Gypsum: A joint tomographic model of mantle density and seismic wave speeds, *J. Geophys. Res.*, *115*, B12310, doi:10.1029/2010JB007631.
Sipkin, S. A., and J. Revenaugh (1994), Regional variation of attenuation and travel time in China from analysis of multiple-ScS phases, *J. Geophys. Res.*, *99*, 2687–2699.
Souriau, A., L. Rivera, A. Maggi, and Lévêque J. J. (2012), Seismic attenuation in the eastern Australian and Antarctic plates, from multiple ScS waves, *Geophys. J. Int.*, *190*, 569–579, doi:10.1111/j.1365-246X.2012.05501.x.
Stein, S., and M. Wysession (2003), *An Introduction to Seismology, Earthquakes, and Earth Structure*, 498 pp., Blackwell Publ., Malden, Mass.
Vallée, M., J. Charléty, A. M. G. Ferreira, B. Delouis, and J. Vergoz (2011), Scardec: A new technique for the rapid determination of seismic moment magnitude, focal mechanism and source time functions for large earthquakes using body wave deconvolution, *Geohys. J. Int.*, *184*, 338–358, doi:10.1111/j.1365-246X.2010.04836.x.
Wessel, P., and W. H. F. Smith (1995), New version of the generic mapping tools released, *Eos Trans. AGU*, *76*, 329–329, doi:10.1029/95EO00198.
Zhou, Y. (2009), Surface-wave sensitivity to 3-D anelasticity, *Geophys. J. Int.*, *178*(3), 1403–1410, doi:10.1111/j.1365-246X.2009.04230.x.